The Global Distribution of Stormtime Geomagnetic Hazards

Jesse Woodroffe[1]

[1]National Aeronautics and Space Administration

November 23, 2022

Abstract

In this study, we present results from an investigation of the spatial variability of geomagnetic disturbances (GMDs) occurring during large (minimum Dst [?] -100 nT) geomagnetic storms. Expanding on a previous study, we quantify the equatorward expansion of extreme GMDs as a function of KP and a new Dst-derived range index, the Disturbance Threshold Indicator (Dti). We then assess the largest GMDs as a function of MLT and MLAT during these storms for different levels of geomagnetic activity and empirically identify intrinsic patterns and systematic variations.

The Global Distribution of Stormtime Geomagnetic Hazards

J. R. Woodroffe[1]

[1]National Aeronautics and Space Administration, 300 Hidden Figures Way SW, Washington, DC 20546

Key Points:

- Stormtime GMD intensities vary with MLT, MLAT, and geomagnetic activity
- Regions affected by extreme GMDs move equatorward during stronger storms
- A *Dst*-based index can quantify the equatorward motion of GMD hazards

Corresponding author: Jesse Woodroffe, `jesse.r.woodroffe@nasa.gov`

Abstract

In this study, we present results from an investigation of the spatial variability of geomagnetic disturbances (GMDs) occurring during large (minimum $Dst \leq -100$ nT) geomagnetic storms. Expanding on a previous study, we quantify the equatorward expansion of extreme GMDs as a function of K_P and a new Dst-derived range index, the Disturbance Threshold Indicator (Dti). We then assess the largest GMDs as a function of MLT and MLAT during these storms for different levels of geomagnetic activity and empirically identify intrinsic patterns and systematic variations.

Plain Language Summary

Ground-level electromagnetic disturbances that impact the power grid (often called GMDs) are most likely to occur during strong geomagnetic storms. The strength of storms is typically measured by two indices, Dst and K_P, and we show that the global intensity and spatial distribution of GMDs can be related to these indices. We find that the regions at risk to GMDs are different for different types of GMDs, and that the extent of these regions expands with increasing geomagnetic activity.

1 Introduction

Severe geomagnetic disturbances (GMDs) and their coupling to critical electrical systems as geomagnetically induced currents (GICs) are a matter of concern to both governments and private sector entities. For systems that normally operate at or near peak capacity, the presence of excess currents driven by external processes can lead to deleterious effects such as reactive power losses, voltage collapse, or even physical component damage (Boteler, 2001).

It is generally observed that extreme GMDs/GICs are minimally dangerous to most power systems except during periods of intense geomagnetic activity when the polar cap expands and the auroral oval moves equatorward. It has long been understood that magnetospheric reconfiguration due to magnetopause reconnection during periods of southward IMF lead to an expansion of the polar cap and the auroral oval; indeed this expansion is a fundamental element of the original substorm picture of Akasofu (1964). Although auroral dynamics thought to be most closely associated with severe GMDs, the traditional measures of auroral activity are not predictive of the latitudinal variation in GMD exposure that is characteristic of the global magnetospheric response to external drivers and thus measures of such activity provide an incomplete picture.

Although Dst is the space weather index most closely associated with geomagnetic storms, the planetary K (K_P) index has a longer history and has been more broadly adopted by operators such as NOAA, who use it as the basis of their "G" scale for geomagnetic storms. A notable and well-recognized shortcoming of K_P is that it may only take on one of 28 discrete values and it saturates at $K_P = 9$, providing no discrimination between a "typical" extreme storm (which occur 1–2 times per solar cycle on average), the March 1989 "Québec" geomagnetic storm, or a "Carrington"-type superstorm (Boteler, 2019).

Because of the limitations of available data for extreme GMD environments, researchers rely on statistical inference to estimate the characteristics that might be observed during as-of-yet unobserved events. A variety of different approaches have been taken for this purpose, including peaks-over-threshold (Thomson et al., 2011; Rogers et al., 2020), block maximum (Woodroffe et al., 2016), and log-normal extrapolation Ngwira et al. (2013); Love, Coïsson, and Pulkkinen (2016). In each case, researchers provided estimates of the 1-in-100 year properties of GMDs. Unfortunately, it is very difficult to verify that such estimates are accurate – despite commendable efforts by modern-day investigators (Love et al., 2019a), there is a paucity of data for historical events of greater intensity than the Québec storm – and, consequently, it should be recognized that our lack of understanding of magnetosphere dynamics during these events fundamentally our ability to reliably infer the behavior or intensity of GMDs during such events.

As a concrete example, it has been suggested by Ngwira et al. (2013) that GMD activity does not intensify below $\lambda \approx 50°$, corresponding to observations from the Québec storm. This conclusion was supported in subsequent work by Love, Pulkkinen, et al. (2016) and Pulkkinen et al. (2019), but as we will later discuss, there are signatures within the historical record which indicate that this "boundary" represents a limitation of the available data rather than the underlying physical processes. Ultimately, it will not possible to fully resolve this issue without either waiting for additional extreme geomagnetic storms or developing reliable physics-based models of the strongly-driven magnetosphere-ionosphere system.

Woodroffe et al. (2016) identified a significant amount of variability in peak magnitudes observed at fixed magnetic latitude (MLAT), which they hypothesized may have been due to magnetic MLT dependence. Such a dependence was previously dismissed as an artifact of station location by Ngwira et al. (2013), but this runs counter to our general understanding of the physical drivers responsible for causing GMDs. For example, Belakhovsky et al. (2019) examined the GICs associated with a variety of specific phenomena, many of which are localized to specific MLT sectors – e.g., sudden commencements (SCs) on the dayside, traveling convection vortices in the morning sector, and magnetic impulse events on the nightside.

Recently, Blake et al. (2021) used historical magnetometer data and numerical simulations to define a quantity called the "maximum extent of the auroral equatorward boundary" (MEAEB). The MEAEB was found to be inversely related to the Dst index according to the formula

$$MEAEB = 33.8° \left(1 - \frac{4.96}{\frac{Dst}{100\ \mathrm{nT}} - 5.84}\right) \quad -1150\ \mathrm{nT} < Dst < 0\ \mathrm{nT} \tag{1}$$

The work by Blake et al. (2021) provides a valuable quantification of the relationship between storm intensity and auroral zone extent. However, the auroral boundary is not uniform in latitude across local times (Carbary, 2005) and intense GMDs are known to be localized (Ngwira et al., 2018), so it is important to understand the relationship between boundary latitudes and GMD intensification.

Rogers et al. (2020) undertook an interesting investigation of this issue, examining the global distribution of exceedance probabilities based on an extreme value theory (EVT) analysis of long time series from a network of magnetometers. This work, which identified the existence of localized regions of strongly-enhanced probability of large GMDs, provides potentially valuable insight into the likelihood of encountering geomagnetic hazards across the globe. However, it is difficult infer local GMD intensities from maps of probabilities, and the application of the EVT methodology requires the temporal isolation of localized peaks through a process known as declustering, thus introducing a filtering effect whereby other nearby peaks are excluded from analysis. It is therefore worthwhile to engage in further analysis of the spatial distribution of GMDs and their intensities as it is important for hazard characterization and is still to a great extent underspecified.

This paper seeks to address two primary questions; (1) What is the global MLAT-MLT distribution of stormtime GMDs intensities? and (2) How does this distribution vary with changes in geomagnetic activity? In order to answer these questions, we will analyze data from hundreds of intense geomagnetic storms. Based on this data, we will determine the global distribution of GMDs to develop global, activity-dependent maps of peak intensity. Using these maps, we will derive a new activity- and MLT-dependent latitudinal boundary for dangerous geomagnetic disturbances. Altogether, these results provide a comprehensive global characterization of the distribution of geomagnetic hazards and their relationship to overall geomagnetic activity.

2 Data

This study is focused on characterizing the spatial distribution of the three fundamental GMDs: horizontal magnetic perturbations, ΔB; the time derivative of the horizontal magnetic field, $\dot{B}$; and the geoelectric field, E. The variation of the spatial distribution of these GMDs with changing levels of geomagnetic activity, as measured by the 3-hour planetary K (K_P) and the hourly Disturbance Storm Time (Dst) indices, will also be investigated.

For this study, we obtained baseline-subtracted 1-minute geomagnetic field data from SuperMAG for all geomagnetic storms with minimum $Dst \leq -100$ nT occurring in the years 1981-2018, an extension of the data set used by Woodroffe et al. (2016). This span includes 237 intervals meeting this criterion, with stormtime minima in the range -589 nT $\leq Dst \leq -100$ nT. A complete listing of events can be found in the supplementary material.

The SuperMAG data files provide geomagnetic fields in a local "NEZ" (North-East-Vertical) geomagnetic coordinate system. In terms of this coordinate system, the GMDs are defined as

$$\Delta B = \sqrt{B_N^2 + B_E^2} \qquad \dot{B} = \sqrt{\dot{B}_N^2 + \dot{B}_E^2} \qquad E = \sqrt{E_N^2 + E_E^2} \tag{2}$$

where a dot over a quantity (e.g., $\dot{B}_N$) denotes the time derivative of that quantity. As indicated in Equation 2, we can directly calculate ΔB from the SuperMAG data; the methods use to calculate $\dot{B}$ and E from magnetic field time series are described in Appendix A. Note that since GMD values may vary by multiple orders of magnitude, it is convenient to deal with the log transform of the GMDs defined by Equation 2.

Each interval in the data set starts at 00:00 UTC on the day during which the storm began (as indicated by either a sudden commencement or a rapid sustained decrease in Dst), and each interval ends at 23:59 UTC on the first day where Dst had recovered by at least 70% from significantly from its stormtime minimum as per the criterion described by Halford et al. (2010). Consequently, this data set also includes some periods, either pre- or post-storm, where geomagnetic activity is relatively quiet. Including these periods has no impact on the calculation of extreme GMDs, but it does allow us to gain insight into how the global patterns of GMD occurrence evolve when going from "quiet time" into "storm time".

3 Analysis

The latitudinal morphology of GMDs has been previously investigated by multiple authors (Ngwira et al., 2013; Woodroffe et al., 2016; Love, Pulkkinen, et al., 2016). Although the specific representations used varied in these studies, the general conclusions were the same – observed GMDs are smallest at low-to-mid latitudes and show enhancement of peak levels above $\sim 45°$ geomagnetic latitude, typically with a peak between $60°$ and $70°$. This is illustrated in Figure 3, which shows the latitudinal profile of the largest GMDs observed at individual magnetometers during each event (one data point per magnetometer per storm).

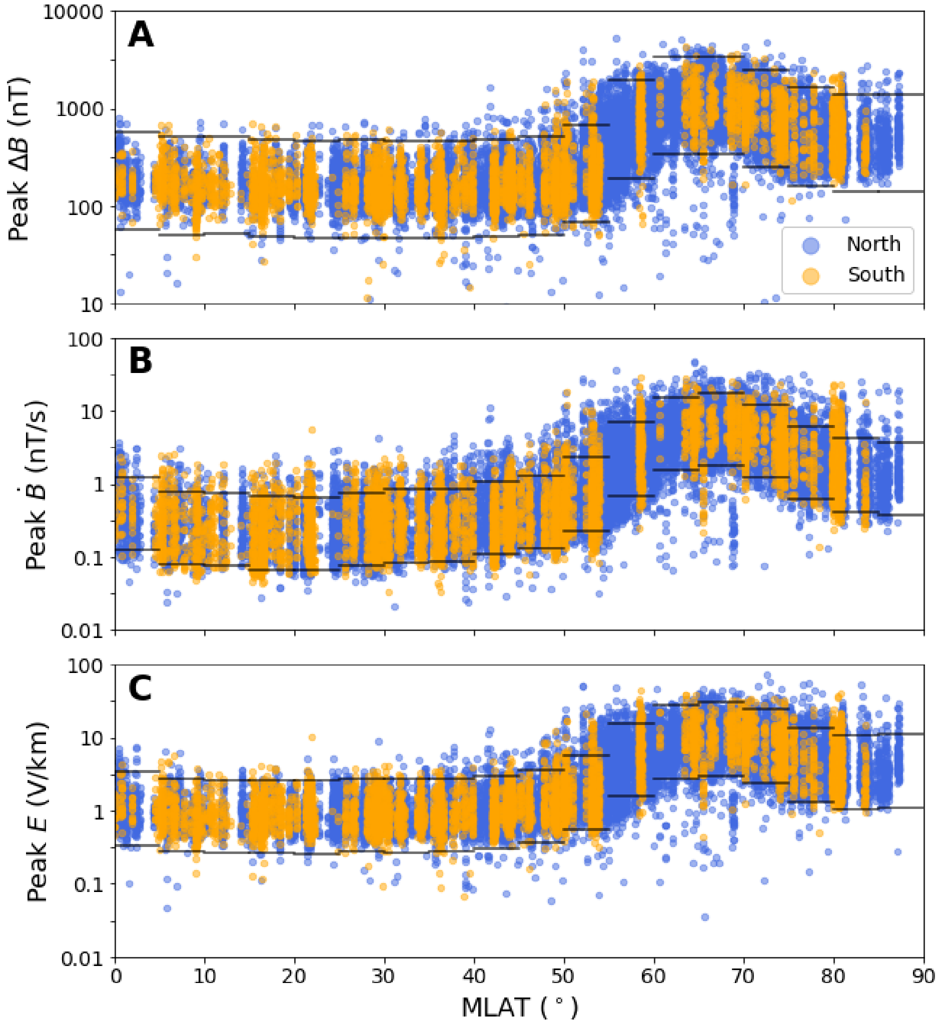

Figure 1. Peak GMD as function of MLAT during the storm events in this study for (A) ΔB; (B) $\dot{B}$; and (C) E. Each symbol denotes the peak value of the corresponding GMD measured at one observatory during a single event and the symbol color denotes the hemisphere of the observatory (blue = northern, orange = southern). In each 5° MLAT section, horizontal black lines demarcate an order-of-magnitude range centered on the median of the data points within that section.

An interesting feature of the GMD profiles, illustrated by stepwise black lines in Figure 3, is that an order of magnitude (or greater) variability is observed at all latitudes, with even more variability observed in the "transition region" between 45° and 60°. This transition-region variability arises from 2 sources: (1) the latitudinal profiles of peak GMD intensities depend on geomagnetic activity, and (2) the latitudinal profiles of peak GMD intensities vary with MLT. We will investigate both of these effects in Sections 3.1 and 3.4, respectively.

3.1 Latitudinal Variation with Peak Geomagnetic Activity

The activity dependence of the latitudinal profile is well illustrated by looking at the location of two characteristic features of the GMD profile, the transition and peak, during individual geomagnetic storms with different peak intensities.

It was previously shown by Woodroffe et al. (2016) that GMDs above 25° MLAT could be well-modeled using a relatively simple parametric form and that, from this form, it was possible to reliably extract a parameter corresponding to the latitude at which GMD magnitudes began to strongly intensify (the transition latitude, λ_T). Quantitatively, we define λ_T as the lowest latitude at which the midpoint value of the GMD profile is obtained, with these values obtained through the process described in B1. Applied to all the storms in our data set, this analysis provides us with 237 Dst-λ_T pairs which, as shown in Figure 3.1, illustrate a clear decrease in λ_T with increasingly negative Dst.

It should be noted that our analyses to this point and hereafter consider only the magnitude of MLAT, not its sign. Neither visual inspection (see Figure 3) nor the two-sample Kolmogorov-Smirnov test give any indication of significant differences between hemispheres, so we have opted to combine the data from both hemispheres.

In order to quantify the activity-dependence of λ_T, we assume a functional form of $\lambda_T = a - b|Dst/100|^c$ and use a robust fitting via least-squares optimization with a "Soft L1" loss function (Virtanen et al., 2020) to determine the coefficients that best represent our data. We repeat this analysis 1000 times using bootstrap resampling and take the median of the results as being the most representative values for each GMD. This analysis leads to find that that λ_T and minimum stormtime Dst are approximately related by

$$\lambda_T(\Delta B) = 68.43° - 11.88° \left| \frac{Dst}{100 \text{ nT}} \right|^{0.33} \tag{3}$$

$$\lambda_T\left(\dot{B}\right) = 68.47° - 12.10° \left| \frac{Dst}{100 \text{ nT}} \right|^{0.32} \tag{4}$$

$$\lambda_T(E) = 68.61° - 12.26° \left| \frac{Dst}{100 \text{ nT}} \right|^{0.32} \tag{5}$$

Thus, for ΔB we have $a = 68.43°$, $b = 11.88°$, and $c = 0.33$; for $\dot{B}$ we have $a = 68.47°$, $b = 12.10°$, and $c = 0.32$; and for E we have $a = 68.61°$, $b = 12.26°$, and $c = 0.32$. As shown in Figure 3.1A–C, these fits do an excellent job of matching the trends of the data; although it is unlikely that this power law to hold for exceptionally large values of Dst, such values are in excess of what is expected for even the "largest imaginable" geomagnetic storm (Vasyliunas, 2011).

Figure 3.1A–C also show the latitude at which the GMD peaks occurs (red symbols and curves, obtained by repeating the above analysis but using the location of the

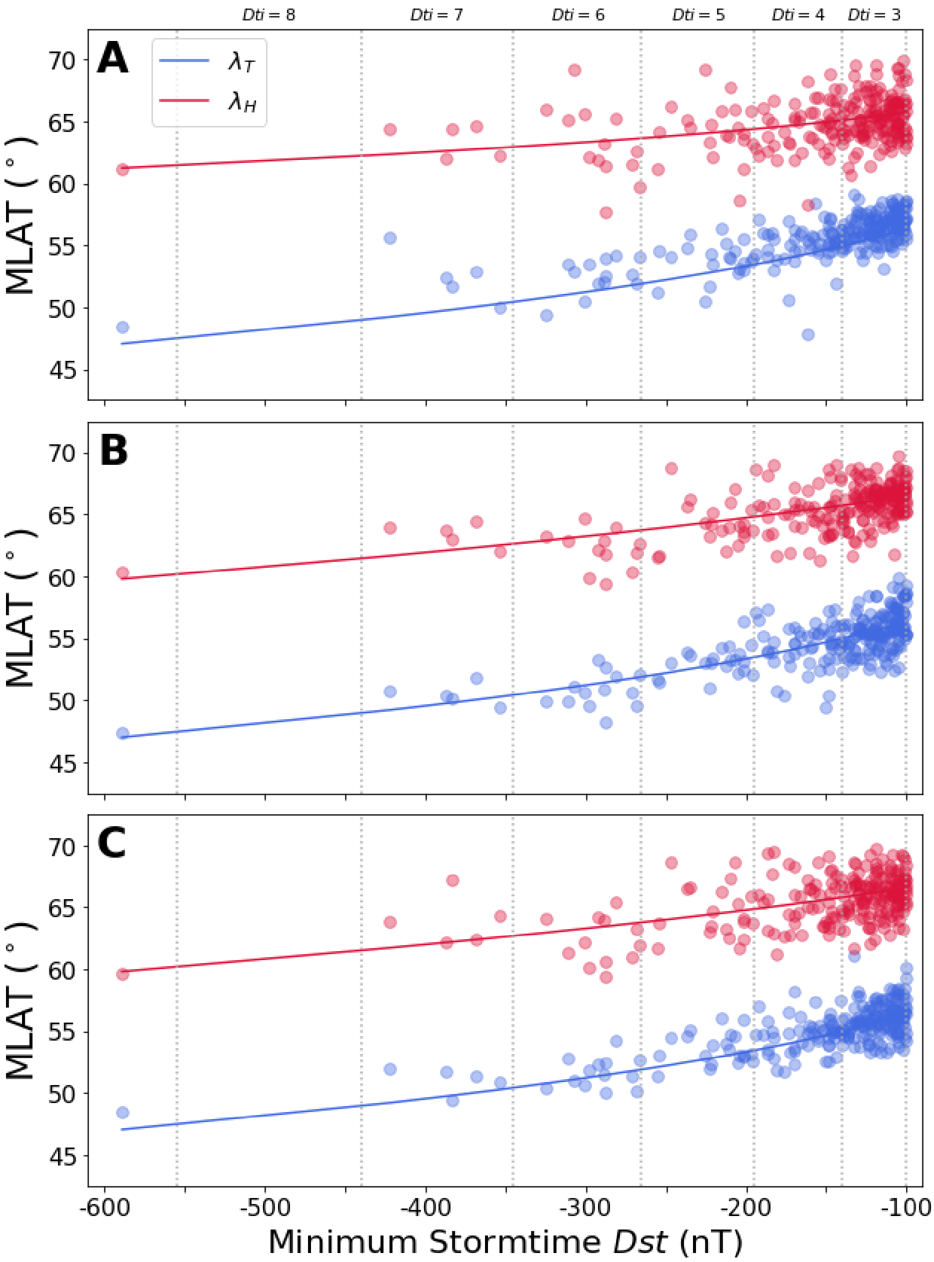

Figure 2. GMD transition latitudes for (A) ΔB, (B) $\dot{B}$, and (C) E. The legend shown in panel A applies to all panels. The vertical dashed lines correspond to increments of 1.5° change in λ_T.

profile's peak, λ_H, instead of λ_T). We find that λ_H also moves equatorward with increasingly negative Dst at roughly the same rate as λ_T, although the parameters of this fit are more variable.

The GMD transition boundaries given by Equations 3–5 are consistently $\sim 2°$ equatorward of the MEAEB, which supports the idea that MEAEB is a reasonable, albeit incomplete, indicator of where intense GMDs are likely to occur.

Although the analysis in this section provides useful insight into the global characteristics of equatorward expansion of GMD activity, it only does so on a very coarse level of detail, reducing all measurements from each geomagnetic storm to a single data point. Moreover, this single number does not really help us to understand the variability observed in Figure 3. Additional insight can be gained by instead looking at the variation of GMDs with respect to temporally finer-grained measures of geomagnetic activity and magnetic local time.

3.2 Activity Measures

For this study, we will characterize geomagnetic activity using two representative indices that are derived from K_P and Dst.

The first index we will use is a "simplified K_P index" that consolidates ranges of K_P into a single central value which we term KS as shown in Table 3.2. The NOAA geomagnetic storm scales are equivalent to $KS = 5 - 9$.

KS	K_P	NOAA
0	$[0^o,\ 0^+]$	-
1	$[1^-,\ 1^+]$	-
2	$[2^-,\ 2^+]$	-
3	$[3^-,\ 3^+]$	-
4	$[4^-,\ 4^+]$	-
5	$[5^-,\ 5^+]$	G1
6	$[6^-,\ 6^+]$	G2
7	$[7^-,\ 7^+]$	G3
8	$[8^-,\ 9^-]$	G4
9	$[9^o]$	G5

Table 1. K_P ranges that define the KS index and the correspondence of this index to the NOAA geomagnetic storm scales. Note that [..., ...] is an interval that starts on the left value (inclusive) and ends on the right value (inclusive).

The second index we use is a new Dst-derived range index, the Disturbance Threshold Indicator (Dti). The purpose of this index, derived in Appendix Appendix C, is to quantify the equatorward motion of GMD hazards as discussed in Section 3.1. The Dti index is defined such that an integer change in the index corresponds to a fixed equatorward movement of the GMD transition latitude by $\Delta\lambda = 1.5°$. Practically speaking, Dti can be interpreted as specifying the equatorward boundary of enhanced GMD activity, λ_{GMD}, which it is related to by $\lambda_{GMD} = 60° - 1.5°Dti$. That is, for a given value of Dti, significant GMDs are most likely to occur at or above the corresponding value of λ_{GMD}. The Dst ranges corresponding to the first 10 values of Dti are shown in Table 3.2 along with the associated values of λ_{GMD}.

Dti	Dst (nT)	λ_{GMD}
0	(-40, ∞]	60.0°
1	(-65, -40]	58.5°
2	(-100, -65]	57.0°
3	(-140, -100]	55.5°
4	(-195, -140]	54.0°
5	(-265, -195]	52.5°
6	(-345, -265]	51.0°
7	(-440, -345]	49.5°
8	(-555, -440]	48.0°
9	(-690, -555]	46.5°

Table 2. Dst ranges that define the Dti index. Note that $(\ldots,\ldots]$ is an interval that starts at the left value (non-inclusive) and ends on the right value (inclusive). For the sake of simplicity, the bounds calculated from Equation (C2) have been rounded to the nearest integer multiple of 5. The corresponding values of λ_{GMD} are given in the right column.

The vast majority of our data set is from periods with $Dti \leq 7$. Indeed, since 1957, only the 1989 Québec storm has ever exceeded $Dti = 7$, ultimately peaking at $Dti = 9$ ($Dst = -589$ nT, $\lambda_{GMD} = 46.5°$). Retrospective studies studies suggest that this threshold would have also been crossed during multiple other events, including the 1921 "Railway" storm ($Dst = -907$ nT, $Dti = 11$, $\lambda_{GMD} = 43.5°$)(Love et al., 2019b) and the 1859 Carrington storm ($Dst = -1760$ nT, $Dti = 15$, $\lambda_{GMD} = 37.5°$)(Tsurutani et al., 2003). Referring to Table 3.2. This is consistent with the oft-cited fact that strong GMDs have been rarely observed below 50° (Ngwira et al., 2013), and it offers a simple explanation for why: there have been no storms events strong enough to drive activity further equatorward than 50°, save for the 1989 Quebéc storm. Given available evidence, this boundary only represents a limitation of the data set.

3.3 Binning and Statistics

If significant MLT structure is present in the distribution of GMD intensities, then looking only at the largest GMD from each station during a given storm would tend to concentrate data points regions of MLT-MLAT space that are associated with strong, potentially localized drivers. This concentration of data points makes it difficult to get good sampling of the entire global distribution by using only per-storm maxima from individual stations and it complicates the assessment of hazards outside of certain high-probability areas.

In order to alleviate the unintentional clustering of data points, we look at the largest GMDs observed in discrete MLT-MLAT sectors, using 24 different MLT bins [0-1),[1-2), ... , [23-24) and 18 different MLAT bins [0°–5°), [5°–10°), ... , [85°–90°]. The values obtained from this analysis are not guaranteed to be the largest that occurred in any given sector during a storm, but they do provide a concrete lower bound for the true maximum. We perform this analysis for a range of geomagnetic activity indicators – $0 \leq KS \leq 8$ and $0 \leq Dti \leq 7$. The result of this is a $24 \times 18 \times 9(8) \times n$-dimensional data set, where $0 \leq n \leq 237$ is a location- and activity-dependent number of events during which measurements in a given sector were available. Specific details of our analysis can be found in Section 3.4.

3.4 GMD Maps

We characterize the GMD data in each MLT-MLAT-actvity bin by estimating the 50^{th} (median) and 95^{th} percentile values of each GMD. Because there is a variable number of points in each bin, this does not directly map to recurrence period, but since $n \leq 237$, the 95^{th} percentile corresponds to once every ≥ 3 years at the average rate of storm occurrence for this data set (see Woodroffe et al. (2016) for a discussion of combining event frequency with probability distributions to estimate recurrence periods). A set of activity-dependent (i.e., $KS = 1 - 9$ and $Dti = 0 - 8$) MLT-MLAT maps for all three types of GMD at both the 50^{th} 95^{th} percentile can be found in the supplementary material.

Figures 3.4 and 3.4 show the 95^{th} percentile GMDs observed during the events in our data set for different levels of geomagnetic activity (maps for the the 50^{th} percentile can be found in the supplementary material). The left, middle, and right columns of each figure show ΔB, $\dot{B}$, and E; the top, middle, and bottom rows show different levels of geomagnetic activity. It is clear from these figures that the severity of geomagnetic disturbances is a strong function of both magnetic latitude and magnetic local time. In all cases, the GMDs are strongest in the late night and morning sectors between 22 and 8 MLT. There is a distinct tendency for stronger GMDs to occur at lower magnetic latitudes near midnight, with the strongest disturbances occurring in many cases below 60° MLAT. Comparing Figures 3.4-3.4, it is also clear that Dti and KS differ in their characterization of expected geomagnetic activity. This is not necessarily surprising given the differences between the observations from which these are derived (low-latitude and mid-latitude, respectively) and the cadences at which they are calculated (1-hour and 3-hour, respectively), but there is nevertheless a strong similarity between the morphology and extent of the regions of enhanced GMD activity that are associated with of KS and Dti.

In order to better quantify the variability of GMD profiles with MLT, we can apply the transition latitude analysis used in Section 3.1 to the GMDs in each MLT sector. These discrete transition points are then used to determine an empirical activity-dependent "GMD oval" using the procedures described in Appendix Appendix B. These GMD ovals, which are plotted on each panel of Figures 3.4 and 3.4, demarcate the low-latitude boundary for extreme GMDs at a given level of geomagnetic activity, with any latitudes above this boundary being exposed to enhanced GMDs during periods of corresponding geomagnetic activity.

A significant difference is evident in the latitudes to which ΔB and the other GMDs extend, with the ΔB oval sometimes being as much as 5° poleward of the corresponding boundaries for $\dot{B}$ or E. This could suggest that that the latter two are associated with localized equatorward-propagating transient phenomena whereas the former is more directly related to electrojet currents and their fluctuations; however, identification of specific physical driving mechanisms is outside the scope of the current study.

Comparing Figures 3.4 and 3.4, we can see that overall GMD intensity appears to be higher for KS than for Dti. The primary cause of this difference is that high-altitude activity is not well-correlated with Dst (which is based on low-latitude magnetic measurements), so the average GMD for a given value of Dti is relatively lower that it would be for a fixed value KS (which incorporates mid-latitude measurements). Our results indicate that KS relates well to both GMD strength and hazard exposure, but – as with K_P – it lacks differentiation at the top end of the scale. For reasons beyond the current analysis, but potentially owing to its smaller time window – 1 hour versus 3 hours – Dti is less well correlated with GMD intensity, but it nevertheless provides a clear measure of latitudinal hazard exposure that is consistent with available data and which is extensible to historical "superstorms" for which KS would provide no distinction relative to weaker events.

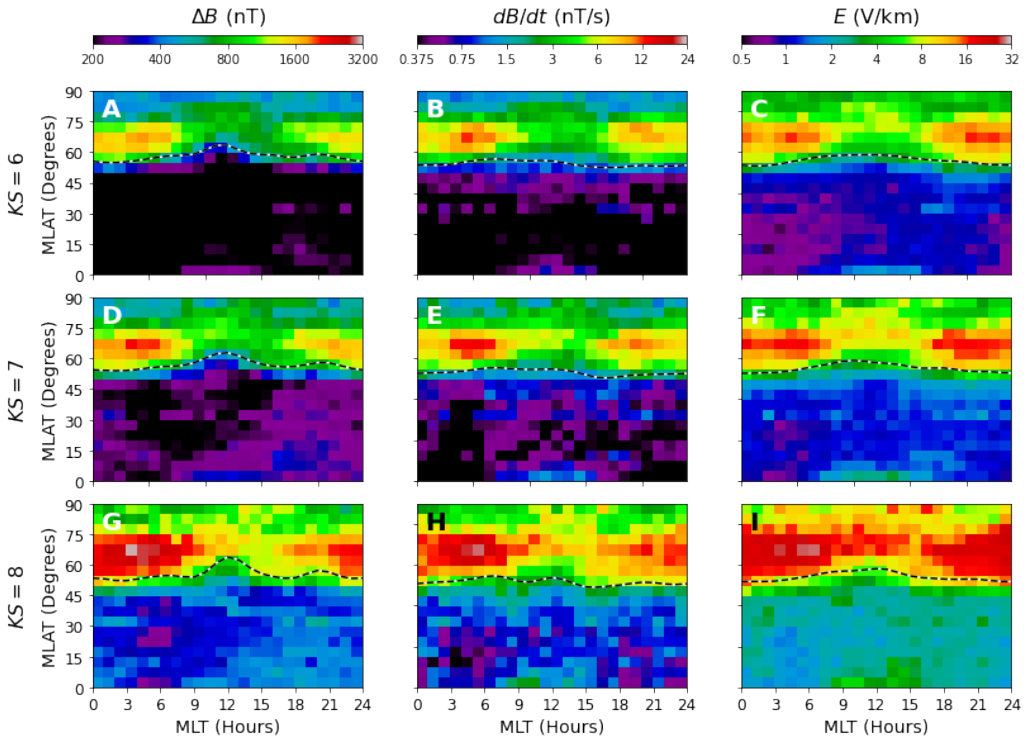

Figure 3. MLT-MLAT distribution of 95$^{\mathrm{th}}$ percentile peak GMDs for different levels of geomagnetic activity: (A) $K_S = 6$; (D-F) $K_S = 7$; (G-I) $K_S = 8$. In each panel, the corresponding KS-dependent λ_T boundary (GMD oval) is indicated by a dashed black line.

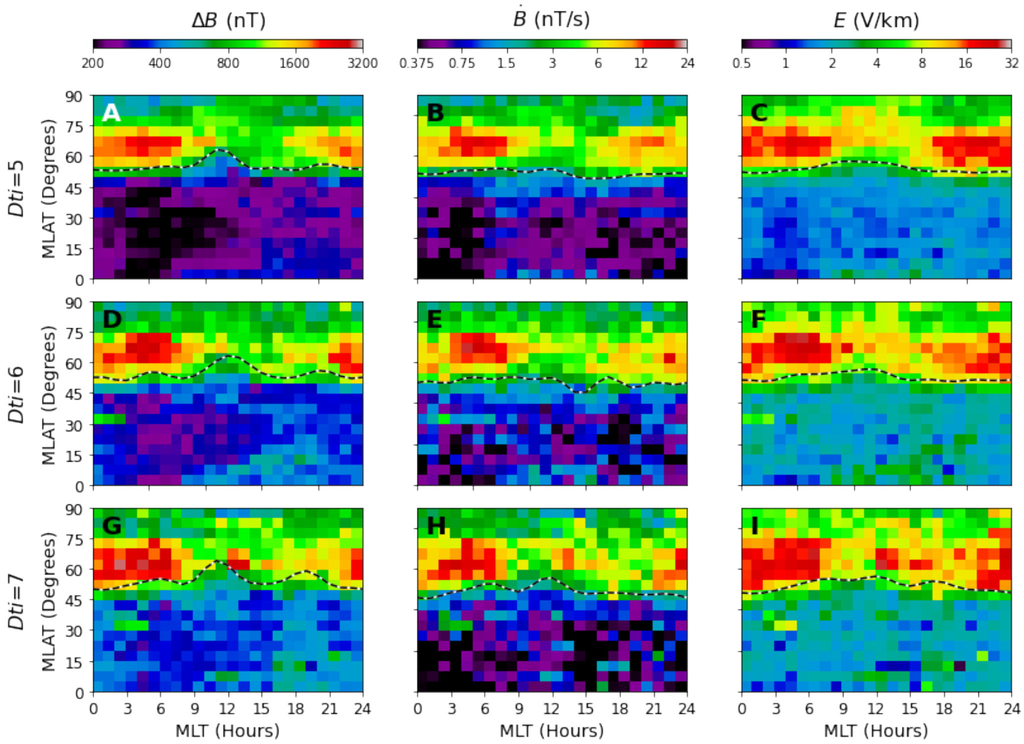

Figure 4. MLT-MLAT distribution of 95[th] percentile peak GMDs for different levels of geomagnetic activity: (A-C) $Dti = 5$; (D-F) $Dti = 6$; (G-I) $Dti = 7$. In each panel, the corresponding Dti-dependent λ_T boundary (GMD oval) is indicated by a dashed black line.

4 Conclusions

This paper provides a comprehensive statistical description of the spatial variability of ground-level electromagnetic disturbances due to space weather. By leveraging a large historical database of geomagnetic data, we are able to characterize variations with respect to a broad range of activity levels and have been able to uncover fundamental characteristics of GMDs that can be used to understand behavior during any type of event.

The results presented in this work demonstrate that there are significant MLT-dependent variations in GMD magnitude during geomagnetic storms. Accounting for activity dependence, MLT variability, and stochastic source properties, we have constructed a global maps of peak stormtime GMDs. These maps explain the observed variability of GMD magnitudes at fixed MLAT, showing that the latitudinal distribution of GMDs varies with both MLT and geomagnetic activity. Consequently, when MLT variability is not explicitly accounted for, the profiles sample many different MLT-dependent distributions and give a range of different intensities for a given MLAT.

Although the severity of geomagnetic storms is conventionally quantified using the Dst index, we have found that this measure alone does not provide adequate context for predicting whether or not extreme GMDs are likely in a given location except at low latitudes. The KS index is found to have a much better association at mid- and high-latitudes than Dst, but this is complicated due to its saturation at $KS = 9$ and poor temporal resolution. This complication can be avoided by using a different measure for the system response, which we demonstrate here using appropriately selected ranges of Dst to define a new index, Dti. Based on the data analyzed in this study, there is no evidence of a fixed latitudinal boundary for GMD intensification; rather, we find that latitudinal extension of this region is well-modeled by a smooth nonlinear function of Dst that is consistent with all observed events. A consequence of this observed relation is that previously-cited limitations on equatorward extent of hazardous GMDs can simply explained by the absence of storms of sufficient intensity to push activity further equatorward.

This study has been largely empirical, but future efforts should focus on the interpretation of our model in terms of fundamental physical processes and drivers. Our results are a clear advance in our understanding of the global distribution of GMDs intensities and their variability. The explanations for our observations relate directly to the evolution of the magnetosphere and its footprint on Earth during extreme geomagnetic storms, and this is an outstanding problem in space weather; a truly complete understanding will require significant advances in our modeling technologies and, quite likely a revolutionary change in our approach to merging models and data through assimilation and machine learning.

Appendix A Time Derivative and Geoelectric Field Calculations

The most accurate method for obtaining geoelectric fields from a measured magnetic field time series is to apply an empirically-determined electromagnetic transfer function (EMTF). Typically, EMTFs are supplied as discrete functions of period or frequency, and they relate the frequency-space geomagnetic disturbance to the frequency-space geoelectric field according to the relationship $\tilde{\mathbf{E}} = \mathcal{Z} \cdot \tilde{\mathbf{B}}$, where a tilde ($\tilde{\ldots}$) indicates the frequency-space representation (obtained, e.g., using a Fourier transform). More explicitly, in terms of the northward and eastward components of the field (as discussed in Section 2),

$$\begin{pmatrix} \tilde{E}_N(\omega) \\ \tilde{E}_E(\omega) \end{pmatrix} = \begin{pmatrix} \mathcal{Z}_{NN}(\omega) & \mathcal{Z}_{NE}(\omega) \\ \mathcal{Z}_{EN}(\omega) & \mathcal{Z}_{EE}(\omega) \end{pmatrix} \cdot \begin{pmatrix} \tilde{B}_N(\omega) \\ \tilde{B}_E(\omega) \end{pmatrix} \tag{A1}$$

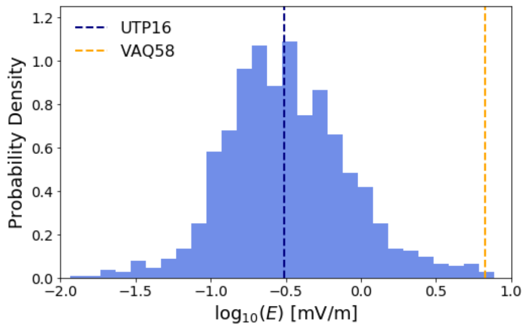

Figure A1. Distribution of peak geoelectric fields generated using for an ensemble of EMTFs with a representative geomagnetic time series. Based on this analysis, a "typical" response is obtained using the UTP16 EMTF and an "extreme" response is obtained using the VAQ58 EMTF.

There have been EMTFs measured at more than a thousand locations across North America, and it is now well understood that the geoelectric response to a given geomagnetic input can vary by orders of magnitude depending on the EMTF. For the purposes of the present study, we are not as interested in the actual geoelectric field that would have been observed at a specific location – but, rather, we want to understand the physically justifiable extreme response. In order to develop sufficient context to understand which EMTFs will provide the desired response, we used data from multiple stations during multiple geomagnetic storms and large set of EMTFs obtained from the IRIS database (Kelbert et al., 2011) to determine statistically representative EMTFs. In doing this analysis, we scale each time series to have a peak magnetic disturbance of 1000 nT and calculate the resultant geoelectric field using all available EMTFs. We then rank the geoelectric field thus obtained and identify the EMTF that produced the consistently strongest response. Figure Appendix A shows the distribution of the geoelectric fields obtained from this procedure along with the location of the representative EMTF responses in this distribution. As indicated in the figure, the most severe response was consistently obtained when using the VAQ58 EMTF(Schultz et al., 2019) (from a survey site near Richmond, VA). We note that the distribution of values in Figure Appendix A shows three orders of magnitude variability are observed between the strongest and weakest geoelectric fields, consistent with the findings of Love, Pulkkinen, et al. (2016). Finally, as an aside, we note that the UTP16 EMTF (from a survey site in central Utah) had the median response, making it the "most representative" EMTF.

It is common to approximate the time derivatives of magnetic fields using a two-point finite difference approximation – e.g., $\dot{B}_N \approx (B_N(t+\Delta t) - B_N(t-\Delta t))/2\Delta t$ – this is almost always an underestimate of the exact derivative. Since, as discussed above, it is necessary for us to operate on the frequency-space representation of the magnetic fields in order to calculate the EMTFs, we can easily obtain a high-accuracy estimate of the magnetic field time derivative via spectral differentiation (i.e., using $\dot{\tilde{B}}_N = -i\omega\tilde{B}_N$). To the extent that we avoid edge effects (which is accomplished using long time series and standard windowing techniques), this approach results in a higher-fidelity estimate of the "true" derivative but does not, in general, yield a significantly different result.

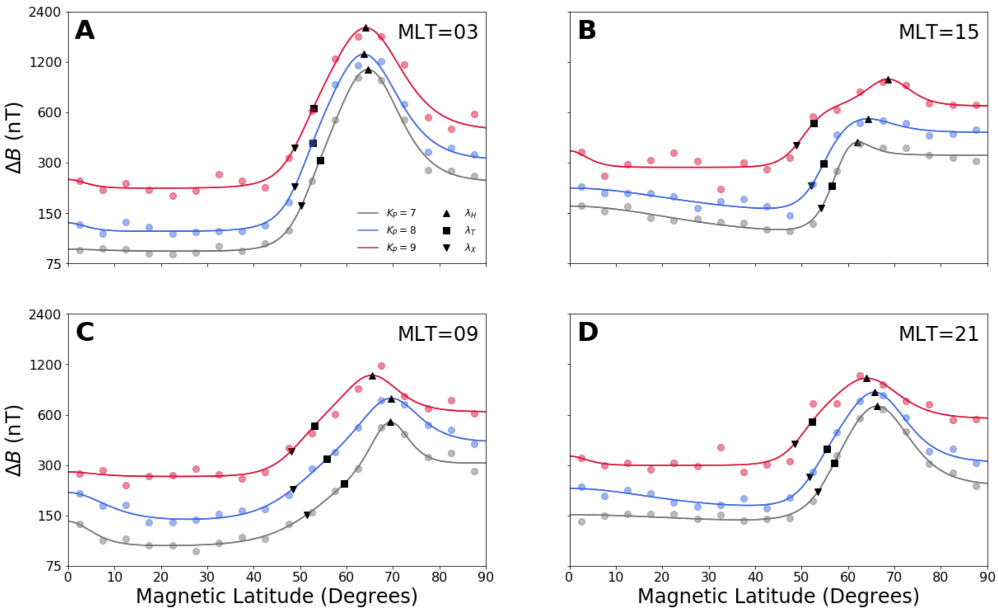

Figure B1. Latitudinal profiles of ΔB with empirical functional fits at different MLTs: (A) MLT=3; (B) MLT=9; (C) MLT=15; (D) MLT=21. Data and fits for $K_S = 7 - 9$ are shown in each of panels A-D and the legend in panel A applies to all. On each profile, the value at λ_T is indicated by a black circle, λ_X is indicated by a downward triangle, and λ_H is indicated by an upward triangle.

Appendix B Profile Models

B1 Latitudinal Profiles

The functional model of Woodroffe et al. (2016) can be generalized to GMD profiles across all latitudes, activities, and local times by specifically including an equatorial electrojet contribution and allowing for the peak of the distribution to be displaced from the transition region. Defining $\xi = \log_{10}(GMD)$, our model is

$$\xi = \frac{\beta + \alpha}{2} + \frac{\beta - \alpha}{2} \tanh\left(\frac{\lambda - \lambda_1}{\Delta\lambda_1}\right) + \delta_0 \operatorname{sech}^2\left(\frac{\lambda}{\Delta\lambda_0}\right) + \delta_2 \operatorname{sech}^2\left(\frac{\lambda - \lambda_2}{\Delta\lambda_2}\right) \tag{B1}$$

where α is the low-latitude baseline, β is the high latitude baseline, $\lambda_{1,2}$ are the mid- and high-latitude enhancement locations, $\delta_{0,2}$ are the magnitudes of the low-latitude and high-latitude enhancements (e.g., equatorial and auroral electrojets), and $\Delta\lambda_{0,1,2}$ are the widths of the equatorial, transition region, and high-latitude profiles. These parameters are determined using robust least-squares optimization with a "Soft L1" loss function. Examples of this fitting function applied to data from different MLTs and activity levels are shown in Figure B1, demonstrating that it is capable of capturing significant profile variability (see e.g., 15 MLT). The transition latitudes for each of these profiles is indicated by a black circle. One interesting point to note is that the transition latitude at 9 MLT actually "retreats" to higher latitudes from $K_P = 8$ to $K_P = 9$, despite the fact that the overall intensity at all latitudes increases.

There are four critical points within each latitudinal profile: λ_L, λ_H, λ_X, and λ_T, which are – respectively – the locations of the minimum and maximum GMD values and the beginning and middle of the transition region. We determine each of these values automatically from the profile fits in the following sequence:

1. First, in order to determine λ_H, we use a minimization algorithm to find the most negative value of $-\xi$ (denoted as ξ_H) and then use a rootfinding algorithm to find the latitude at which this value is obtained; λ_2 is a very good first guess, and it guaranteed to lie on the interval $0° \leq \lambda \leq 90°$.
2. Second, in order to determine λ_L, we repeat the procedure used for λ_H, but instead minimize ξ (denoted by ξ_L); for the purposes of rootfinding, a good first guess is $\lambda_H/2$, and it is guaranteed to lie on the interval $0° \leq \lambda_L < \lambda_H$.
3. Third, in order to determine λ_T, we use rootfinding to determine the latitude at which $\xi = (\xi_L + \xi_H)/2$; a good first guess is λ_1, and it is guaranteed to lie on the interval $\lambda_L < \lambda_T < \lambda_H$.
4. Fourth, in order to determine λ_X, we repeat the procedure used for λ_T, but instead determine the latitude at which $\xi = (3\xi_L+\xi_H)/4$; an empirically-determined good first guess is $\lambda_T - 5°$, and it is guaranteed to lie on the interval $\lambda_L < \lambda_X < \lambda_T$.

B2 Magnetic Local Time Profiles

We model the MLT-variability of geomagnetic disturbance boundaries (ovals) using a sixth-order Fourier series expansion,

$$\lambda_q(GMD) = \sum_{m=0}^{6} \left(A_m \cos(m\varphi) + B_m \sin(m\varphi)\right) \tag{B2}$$

where $q = L, X, T, H$ indicates the particular latitudinal quantity being modeled (such as the transition or peak). The coefficients of each fit are determined using the same robust method described in B1.

Appendix C Definition of the *Dti* Index

We derive the Dti index from the model described in Section 3.1 and its basic functional ansatz, a power law that links Dst with λ_T:

$$\lambda_T = a - b\left|\frac{Dst}{100\ \text{nT}}\right|^c \tag{C1}$$

In order to use Equation (C1), we must choose particular values for a, b, and c. Although each type of GMD had different values for these parameters, they were nevertheless generally similar, so we simply average them to find $a = 68.43°$, $b = 12.08°$ and $c = 0.32$.

Because Dti is intended to be a measure of stormtime disturbance, we set its baseline value, $Dti = 0$, at the threshold intensity for defining geomagnetic storms, $Dst = -40$ nT. Specifically, we define Dti such that each integer value corresponds to a uniform change in λ_T. Using the given functional parameters, we get $\lambda_T = 59.44° \approx 60°$ for $Dti = 0$. We thus can write $\lambda_T = 60° - Dti\Delta\lambda$. In order to relate Dti back to Dst, we must first choose an appropriate value for $\Delta\lambda$.

Using Equation (C1) with a baseline at -40 nT, it follows that the value of Dst at which λ_T decreases by $n\Delta\lambda$ relative to its baseline is

$$Dst_n = -100\left(\left(\frac{40}{100}\right)^c - \frac{n\Delta\lambda}{b}\right)^{\frac{1}{c}}\ \text{nT} \tag{C2}$$

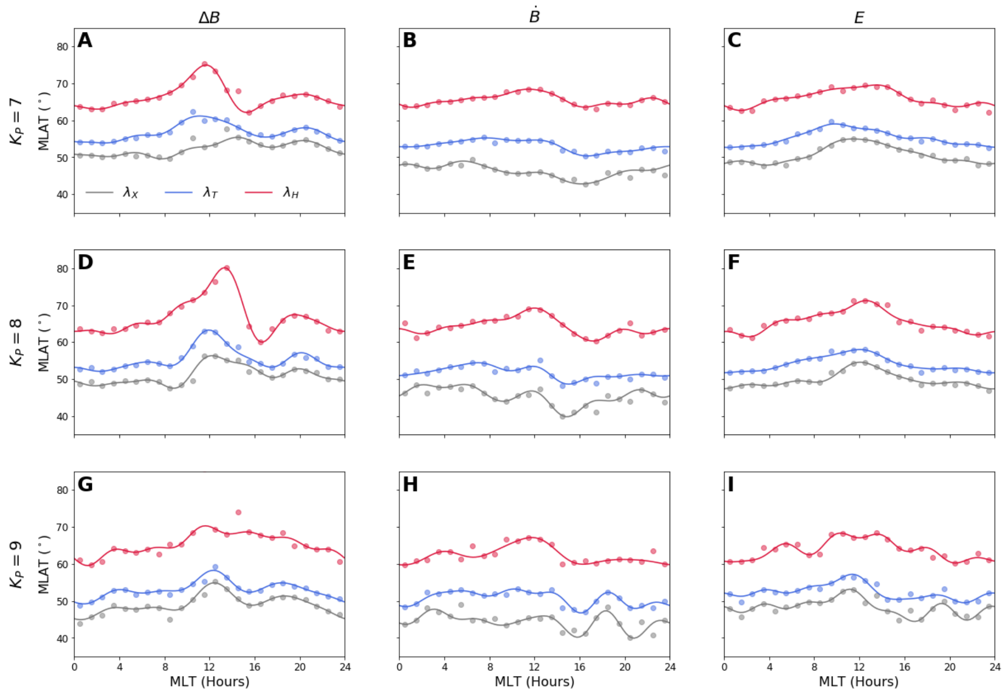

Figure B2. Example GMD ovals for (left column) ΔB; (middle column); $\dot{B}$; and (right column) E. In each row, both fitted ovals (solid line) and original data (points) are shown for a fixed value of K_P, (top row) $K_P = 7$; (middle row) $K_P = 8$; (bottom row) $K_P = 9$. All panels share the legend in Panel A.

Given no a priori reason to choose any particular value of $\Delta\lambda$, it is tempting to simply use $\Delta\lambda = 1°$. However, the extent of the historical data and number of storms in our data set makes it useful to have a larger value, as it allows for more events to be gathered within each classification level. We have chosen to adopt $\Delta\lambda = 1.5°$, as geomagnetic storm for which Dst data is available thus fall nicely within the range $[0 \leq Dti \leq 9]$, the same number of categories as the KS index. It is important to note that there is no direct correspondence between the geomagnetic conditions represented by similar values of KS and Dti, and that there are higher values of Dti that can be derived from Equation C2, potentially allowing it to be extended to characterize more extreme events than KS.

Acknowledgments

The Python code and notebooks used for analysis and figure generation are available on Zenodo at https://doi.org/10.5281/zenodo.5148759. The K_P geomagnetic index was obtained from GFZ Potsdam, https://www.gfz-potsdam.de/en/kp-index/. The Dst geomagnetic index was obtained from the WDC for Geomagnetism, http://wdc.kugi.kyoto-u.ac.jp/dstdir/. Electromagnetic transfer functions were obtained from the IRIS SPUD database, http://ds.iris.edu/spud/emtf. The ground magnetometer data were obtained from SuperMAG, http://supermag.jhuapl.edu. We gratefully acknowledge contributions from the SuperMAG collaborators: Intermagnet; USGS, Jeffrey J. Love; CARISMA, PI Ian Mann; CANMOS; The S–RAMP Database, PI K. Yumoto and Dr. K. Shiokawa; The SPIDR database; AARI, PI Oleg Troshichev; The MACCS program, PI M. Engebretson, Geomagnetism Unit of the Geological Survey of Canada; GIMA; MEASURE, UCLA IGPP and Florida Institute of Technology; SAMBA, PI Eftyhia Zesta; 210 Chain, PI K. Yumoto; SAMNET, PI Farideh Honary; The IMAGE magnetometer network, PI L. Juusola; AUTUMN, PI Martin Connors; DTU Space, PI Anna Willer; South Pole and McMurdo Magnetometer, PI's Louis J. Lanzarotti and Alan T. Weatherwax; ICESTAR; RAPIDMAG; British Antarctic Survey; McMac, PI Dr Peter Chi; BGS, PI Dr Susan Macmillan; Pushkov Institute of Terrestrial Magnetism, Ionosphere and Radio Wave Propagation (IZMIRAN); GFZ, PI Dr Juergen Matzka; MFGI, PI B. Heilig; IGFPAS, PI J. Reda; University of L'Aquila, PI M. Vellante; BCMT, V. Lesur and A. Chambodut; Data obtained in cooperation with Geoscience Australia, PI Marina Costelloe; AALPIP, co-PIs Bob Clauer and Michael Hartinger; SuperMAG, PI Jesper W. Gjerloev; Sodankylä Geophysical Observatory, PI Tero Raita; Polar Geophysical Institute, Alexander Yahnin and Yarolav Sakharov; Geological Survey of Sweden, Gerhard Schwartz; Swedish Institute of Space Physics, Mastoshi Yamauchi; UiT the Arctic University of Norway, Magnar G. Johnsen; Finnish Meteorological Institute, PI Kirsti Kauristie.

References

Akasofu, S.-I. (1964). The development of the auroral substorm. *Planetary and Space Science*, *12*, 273–282. doi: 10.1016/0032-0633(64).90151-5

Belakhovsky, V., Pilipenko, V., Engebretson, M., & Sakharov, Y. (2019). Impulsive dusturbances of the geomagnetic field as a cause of induced currents of electrical power lines. *Journal of Space Weather and Space Climate*, *9*. doi: 10.105/swsc/2019015

Blake, S., Pulkkinen, A., Schuck, P., Glocer, A., & Tóth, G. (2021). Estimating maximum extent of auroral equatorward boundary using historical and simulated surface magnetic field data. *Journal of Geophysical Research: Space Physics*, *126*. doi: 10.1029/2020JA028284

Boteler, D. H. (2001). Space weather effects on power systems. In P. Song, H. J. Singer, & G. L. Siscoe (Eds.), *Space weather (geophysical monograph 125)* (chap. 39). Washington, D.C.: American Geophysical Union.

Boteler, D. H. (2019). A 21st century view of the march 1989 magnetic storm. *Space*

Weather, *17*(10), 1427–1441. doi: doi:10.1029/2019SW002278

Carbary, J. (2005). *A kp-based model of auroral boundaries* (Vol. 3). doi: 10.1029/2005SW000162

Halford, A., Fraser, B., & Morley, S. (2010). Emic wave activity during geomagnetic storm and nonstorm periods: Crres results. *Journal of Geophysical Research*, *115*. doi: 10.1029/2010JA015716X

Kelbert, A., Egbert, G. D., & Schultz, A. (2011). Iris dmc data services products: Emtf, the magnetotelluric transfer functions. doi: 10.17611/DP/EMTF.1

Love, J. J., Coïsson, P., & Pulkkinen, A. (2016). Global statistical maps of extreme-event magnetic observatory 1 min first differences in horizontal intensity. *Geophysical Research Letters*, *43*, 4126–4135. doi: 10.1002/2016GL068664

Love, J. J., Hayakawa, H., & Cliver, E. W. (2019a). Intensity and impact of the new york railroad superstorm of may 1921. *Space Weather*, *17*, 1281-1292. doi: 10.1029/2019SW002250

Love, J. J., Hayakawa, H., & Cliver, E. W. (2019b). Intensity and impact of the new york railroad superstorm of may 1921. *Space Weather*, *17*(8), 1281–1292. doi: doi:10/1029/2019SW002250

Love, J. J., Pulkkinen, A., Bedrosian, P., Jonas, S., Kelbert, A., Rigler, E. J., … Black, C. E. (2016). Geoelectric hazard maps for the continental united states. *Geophysical Research Letters*, *43*(18), 9415-9424. doi: 10.1002/2016GL070469

Ngwira, C., Pulkkinen, A., Wilder, F., & Crowley, G. (2013). Extended study of extreme geoelectric field event scenarios for geomagnetically induced current applications. *Space Weather*, *11*, 121–131. doi: 10.1002/swe.20021

Ngwira, C., Sibeck, D., Silveira, M., Georgiou, M., Weygand, J., Nishimura, Y., & Hampton, D. (2018). A study of intense local db/dt variations during two geomagnetic storms. *Space Weather*, *16*, 676-693. doi: 10.1029/2018SW001911

Pulkkinen, A., Schuck, P., & Blake, S. (2019). *Review of peer-reviewed research regarding the effects of geomagnetic latitude on geoelectric fields* (Tech. Rep. No. 3002016885). Electric Power Research Institute.

Rogers, N. C., Wild, J. A., Eastoe, E. F., Gjerloev, J. W., & Thomson, A. W. P. (2020). A global climatological model of extreme geomagnetic field fluctuations. *Journal of Space Weather and Space Climate*, *10*(5). doi: 10.1041/swsc/2020008

Schultz, A., Egbert, G. D., Kelbert, A., Peery, T., Clote, V., Fry, B., & Erofeeva, S. (2019). Usarray ta magnetotelluric transfer functions. doi: 10.17611/DP/EMTF/USARRAY/TA

Thomson, A. W., Dawson, E. B., & Reay, S. J. (2011). Quantifying extreme behavior in geomagnetic activity. *Space Weather*, *9*(S10001). doi: 10.1029/2011SW000696

Tsurutani, B., Gonzalez, W. D., Lakhina, G. S., & Alex, S. (2003). The extreme magnetic storm of 1859. *Journal of Geophysical Research*, *108*. doi: 10.1029/2002JA009504

Vasyliunas, V. (2011). The largest imaginable magnetic storm. *Journal of Solar-Terrestrial Physics*, *73*, 1444-1446. doi: 10.1016/j.jastp.2010.05.012

Virtanen, P., Gommers, R., & et al., T. O. (2020). Scipy 1.0: Fundamental algorithms for scientific computing in python. *Nature Methods*, 261-272. doi: 10.1038/s41592-019-0686-2

Woodroffe, J. R., Morley, S. K., Jordanova, V. K., Henderson, M. G., Cowee, M. M., & Gjerloev, J. G. (2016). The latitudinal variation of geoelectromagnetic disturbances during large (dst≤-100 nt) geomagnetic storms. *Space Weather*, *14*(9), 668-681. doi: 10.1002/2016SW001376